Journal of Nuclear Materials 459 (2015) 53–61

Contents lists available at ScienceDirect

Journal of Nuclear Materials

journal homepage: www.elsevier.com/locate/jnucmat

# Microstructural characterizations of 14Cr ODS ferritic steels subjected to hot torsion

A. Karch [a,b,*], D. Sornin [a], F. Barcelo [a], S. Bosonnet [a], Y. de Carlan [a], R. Logé [c]

[a] CEA, DEN, Service de Recherches Métallurgiques Appliquées, 91191 Gif-sur-Yvette, France
[b] Centre de mise en forme des matériaux (CEMEF), Mines Paris-tech, CNRS UMR 7635, BP 207, 1 rue Claude Daunesse, 06904 Sophia Antipolis Cedex, France
[c] Laboratory of Thermomechanical Metallurgy – PX Group Chair, Ecole Polytechnique Fédérale de Lausanne (EPFL), Rue de la Maladière 71b – CP 526, CH-2002 Neuchâtel, Switzerland

ARTICLE INFO

*Article history:*
Received 15 April 2014
Accepted 22 December 2014
Available online 9 January 2015

ABSTRACT

Oxide dispersion strengthened (ODS) steels are very promising materials for nuclear applications. In this paper, the hot working behavior of ODS ferritic steels, consolidated by hot extrusion, is studied through torsion tests. Three ODS steels are produced acting on both the quantity of Ti and $Y_2O_3$ added to the matrix (wt% Fe–14Cr–1W), and the density and size of the nanoparticles. A temperature range of 1000–1200 °C and strain rates from $5 \cdot 10^{-2}$ to $5\ s^{-1}$ are considered. The microstructures of deformed samples are examined by Electron Back-Scatter Diffraction and X-ray diffraction techniques. It is observed that hot plastic strain leads to an early damage with nucleation and growth of cavities along grain boundaries. Except for the damage, very few microstructural and textural evolutions are noticed. The three tested ODS steels exhibit almost the same behavior under hot torsion straining, regardless of the precipitation state. Overall, the experimental results are interpreted through a mechanism of strain accommodation at grain boundaries, with low dislocation activity in the bulk of the grains.

© 2014 Elsevier B.V. All rights reserved.

## 1. Introduction

Oxide dispersion strengthened (ODS) Ferritic steels (12–18 wt%Cr) offer great potential as fuel cladding in sodium-cooled fast reactors (SFR) [1–3]. Compared with austenitic steels, they exhibit an excellent resistance to swelling under irradiation thanks to their bcc structure [4]. The nanosized and thermally stable oxide particles (Y–Ti–O) in these alloys provide good creep strength at high temperature [5]. Indeed, the very fine precipitates can be effective barriers to the motion of dislocations under service conditions [6].

The production of ODS steels usually involves powder metallurgy methods including mechanical alloying and subsequent powder consolidation using either hot extrusion (HE) or hot isostatic pressing (HIP) [7]. During HE process, the materiel undertakes a severe plastic deformation leading to a complex microstructure, which consists of a mixture of elongated grains with a specific orientation ⟨110⟩ parallel to the extrusion direction, and relatively equiaxed and randomly oriented small grains [8–10]. The microstructural anisotropy is more pronounced in the ODS ferritic grades (>wt%12Cr) than in martensitic ones [11,12]. Understanding the metallurgical phenomena which may occur during HE and lead to the observed microstructure is a key issue in order to produce materials with appropriate properties. The dynamic recrystallization which may occur during hot working is of particular interest.

This work investigates the microstructure evolution during hot torsion tests. Hot torsion tests are chosen to mimic the thermomechanical loading applied during the HE of ODS ferritic stainless steels. The microstructure after high-temperature deformation is characterized by Electron Back-Scatter Diffraction (SEM-EBSD) and X-Ray Diffraction (XRD) in order to determine the grain morphology and crystallographic texture. This study also provides a useful first dataset to identify the rheology of the material, at high temperatures and large strains, which can be used for the numerical simulation of the hot extrusion process.

## 2. Experimental procedure

### 2.1. Materials and torsion test procedure

In the present study, two ODS ferritic stainless steel powders were used. Their chemical compositions in weight percentage are given in Table 1.

Two gas-atomized pre-alloyed powders, produced by *Aubert&Duval*, were mechanically alloyed with $Y_2O_3$ or $Y_2O_3 + TiH_2$ particles, in an attritor under hydrogen atmosphere by the Austrian

* Corresponding author at: CEA, DEN, Service de Recherches Métallurgiques Appliquées, 91191 Gif-sur-Yvette, France.
*E-mail address:* abdellatif.karch@gmail.com (A. Karch).

http://dx.doi.org/10.1016/j.jnucmat.2014.12.104
0022-3115/© 2014 Elsevier B.V. All rights reserved.

**Table 1**
Composition (%wt) in major elements of studied materials.

| Reference | Fe | Cr | W | Ti | $Y_2O_3$ |
|---|---|---|---|---|---|
| Powder 1 | Bal. | 14 | 1 | 0.4 | 0.3 |
| Powder 2 | Bal. | 14 | 1 | 0.3 | 0.25 |

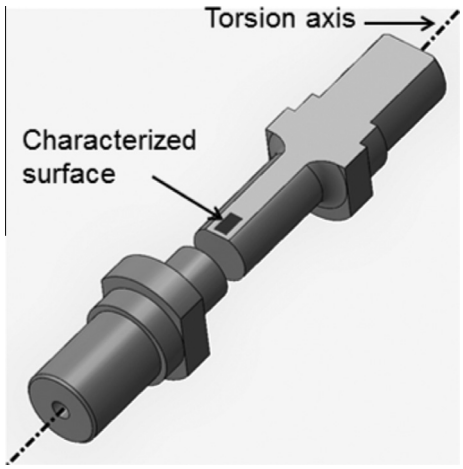


**Fig. 1.** Description of the flat surface used for microstructural analysis.

company *PLANSEE* to form the powders 1 and 2, respectively. Powder 1 (mean particle size of about 80 μm) was put into a low carbon steel can and vacuumed at 400 °C during 2 h under $2 \cdot 10^{-5}$ mBar. Then, the billet was heated in air at 1100 °C for 1 h and consolidated by Hot Uniaxial Pressing (HUP) to form the material 1. HUP consists in an interrupted hot extrusion process that leaves a part of the material in the upstream of the die. Therefore, in this region the material is consolidated only by the uni-axial movement of the ram. It has been shown that this state is fully dense and presents a uniform microstructure without preferential crystallographic texture [13].

From the powder 2, two materials were produced: material 2 and material 3; the first one with the same procedure as described above, and the second one was heat treated at 1350 °C for 3 h under $7 \cdot 10^{-5}$ mBar vacuum before the consolidation process. The obtained consolidated materials (Table 2) were then used to prepare torsion test samples. First, 10 mm cylindrical rods were cut by Electric Discharge Machining (EDM). Specimens, with a gauge length of 11.6 mm and a diameter of 4.5 mm, were then machined from this base material (Fig. 1). Those dimensions are smaller than the standard torsion sample geometry. However, the very fine microstructure of ODS alloys is not expected to lead to geometry effects.

Torsion tests usually allow reaching large strains before plastic instability occurs. Temperatures from 1000 to 1200 °C and strain rates from 0.05 to 5 $s^{-1}$ were considered. Those temperatures simulate the conditions commonly used in the HE of ODS steels. Nevertheless, the selected strain rate values remain lower than those in HE, which can reach 25 $s^{-1}$ [14]. The samples were introduced in a quartz tube with argon flow to ensure protection against oxidation, and were heated with a lamps furnace. The temperature during the torsion test was measured by a thermocouple placed in the head of the sample. After deformation, the samples were immediately water quenched in order to retain the deformation microstructure.

The measurements during the torsion tests provide the torque $\Gamma$ vs. the number of turns $N$. The equivalent stress $\bar{\sigma}$ and strain $\bar{\varepsilon}$ were calculated using the Fields and Backofen analysis [15] through the following equations:

**Table 2**
Condition of manufacturing of studied materials.

| Reference | Initial powder | Heat treatment before consolidation | Consolidation process |
|---|---|---|---|
| Material 1 | Powder 1 | 1100 °C/1 h | HUP |
| Material 2 | Powder 2 | 1100 °C/1 h | HUP |
| Material 3 | Powder 2 | 1350 °C/3 h + 1100 °C/1 h | HUP |

$$\bar{\sigma}(R) = \frac{\Gamma\sqrt{3}}{2\pi R^3}(3 + m + \theta) \quad \text{with} \begin{cases} m = \left(\frac{\partial \ln \Gamma}{\partial \ln N}\right)_{N=cte} \\ \theta = \left(\frac{\partial \ln \Gamma}{\partial \ln N}\right)_{\dot{N}=cte} \end{cases} \tag{1}$$

$$\bar{\varepsilon}(R) = \frac{2\pi N}{\sqrt{3}L} R \tag{2}$$

where $\Gamma$ is the torque (N m), $N$ number of turns, $R$ the sample radius, $L$ the gauge length, $m$ the strain sensitivity and $\theta$ the work hardening exponent.

### 2.2. Microstructural investigations

Metallurgical examinations were carried out on tangential sections (parallel to the torsion axis) at a distance of 0.8$R$ from the torsion axis, $R$ being the radius of the gauge length as illustrated in Fig. 1.

Microstructure and local crystallographic orientations of deformed samples were examined by EBSD and XRD techniques. For this purpose, the flat surface of torsion samples was mechanically polished up to a roughness of 1 μm. Final mechanical polishing with a solution consisting of colloidal silica (OP-S, 90 vol.%) and $H_2O$ (10 vol.%) was then performed for 6 h.

EBSD measurements were carried out on a JEOL 7001-FLV scanning electron microscope equipped with Field Emission Gun and operating at an accelerating voltage and working distance of 20 KV and 15 mm, respectively. EBSD analysis was performed both on as-received materials and deformed samples at various temperatures and a strain rate of 0.05 $s^{-1}$. The strain rate was considered to be low enough to avoid significant warming due to plastic dissipation. Therefore, isothermal conditions were assumed. For the material 1, torsion tests were carried out up to $\bar{\varepsilon} = 0.4$, corresponding to the peak of the flow stress, and also until fracture. This interrupted test allows to determine the effect of the applied strain on the microstructure. The EBSD mapped areas were $60 * 45$ $\mu m^2$, and the chosen step size was 50 nm. The Bruker software was used for the data acquisition, and the HKL software (Oxford Instruments) for the data analysis. In this study, microstructures are shown using a color-coded orientation (i.e. inverse pole figure with the torsion axis projected in the standard stereographic triangle). The shearing direction is indicated in the up-right corner of each figure.

XRD investigations were performed on four deformed samples of material 1, in order to get more global information on the microstructure, using a Bruker D8-Discover goniometer, operating with the Copper Kα radiation ($\lambda_{K\alpha 1} = 1.5405$ nm; $\lambda_{K\alpha 2} = 1.5443$ nm). A Ni-filter was used to reduce the background noise. The diffracted radiation was collected by a rapid Lynxeye detector, and the analysis was done in $\theta - 2\theta$ configuration.

## 3. Results and discussion

### 3.1. Hot torsion tests

For the material 1, the flow curves obtained for different conditions are reported in Fig. 2. The flow stress is, as expected,

increasing with strain rate and dropping with temperature. A rapid strain hardening followed by a weak softening is noticed.

The flow stress is in the range of 60–280 MPa under the tested conditions. Compared to a standard ferritic stainless steel (AISI 430 material) deformed in the same conditions, these values are much higher. The observed ductility, however, is lower [16].

The ductility of ODS steels is limited during hot deformation, due to nanoparticles strengthening and also to the limited grain boundary migration as a consequence of Zener pinning effects.

The flow stress is temperature and strain rate dependent, and often found to obey a power relationship with strain rate and an Arrhenius type law with temperature:

$$\sigma_{\text{peak}} = A\dot{\varepsilon}^m . \exp\left(\frac{Q}{RT}\right) \quad (3)$$

$A$ being an empirical constant, $m$ the strain rate sensitivity, $Q$ the apparent activation energy for deformation and $R$ the gaz constant, equal to 8.314 J/mol K.

The calculated values of $m$ and $Q$ in the tested conditions are about 0.1 and 71.4 KJ/mol, respectively. Strain rate and temperature sensitivity of the studied material are slightly different from those of the commercial grade AISI 430 stainless steel (0.23 and 83.5 KJ/mol respectively) [16]; in particular the strain rate sensitivity is lower, which is consistent with the reduced ductility.

Fig. 3 shows the evolution of strain to failure with temperature at various strain rates. It can be seen that ductility increases with increasing temperature for all strain rates. From 0.05 $s^{-1}$ to 0.5 $s^{-1}$ conditions, the ductility increases with increasing strain rate, but at 5 $s^{-1}$, this tendency is not confirmed in the low temperature range. A peak of ductility is observed at 1200 °C and 5 $s^{-1}$. The ductility increase with strain rate was already reported by other studies through tensile tests at temperatures up to 750 °C and strain rates between $10^{-5}$ and $5 \cdot 10^{-2}$ $s^{-1}$ [9,17]. However, in the torsion conditions, the rising temperature induced by plastic dissipation, especially at high strain rates, may explains the increase ductility observed in Fig. 3.

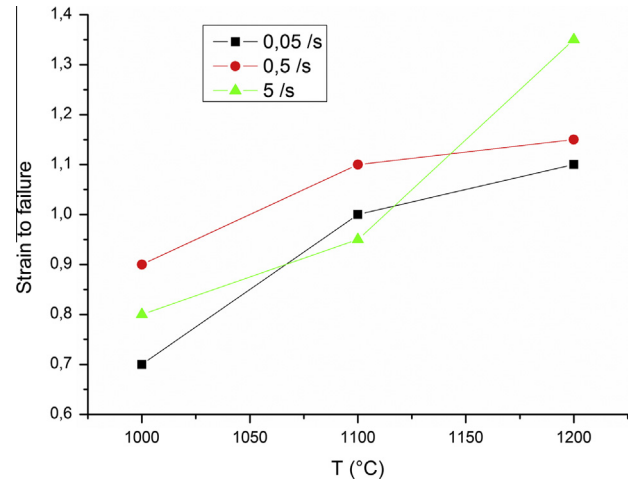


**Fig. 3.** Strain to failure obtained in various torsion test conditions for material 1.

Table 3 presents a comparison between the peak flow stress and strain to failure obtained at two temperatures (1000 °C and 1200 °C), and at 0.05 $s^{-1}$, for the three investigated materials.

Material 3 presents almost the same flow stress as material 2, but its ductility is twice lower for both temperatures. The very long heat treatment before the consolidation process is here shown to be detrimental to the ductility of the ODS material. Indeed, it leads to the formation of strings mainly composed of Ti-oxides of a few hundred nm, as pointed by red arrows in the SEM image of Fig. 4. Those strings are located at the Prior Particle Boundaries (PPBs) of about 40–80 μm in size. Under deformation, the induced porosities

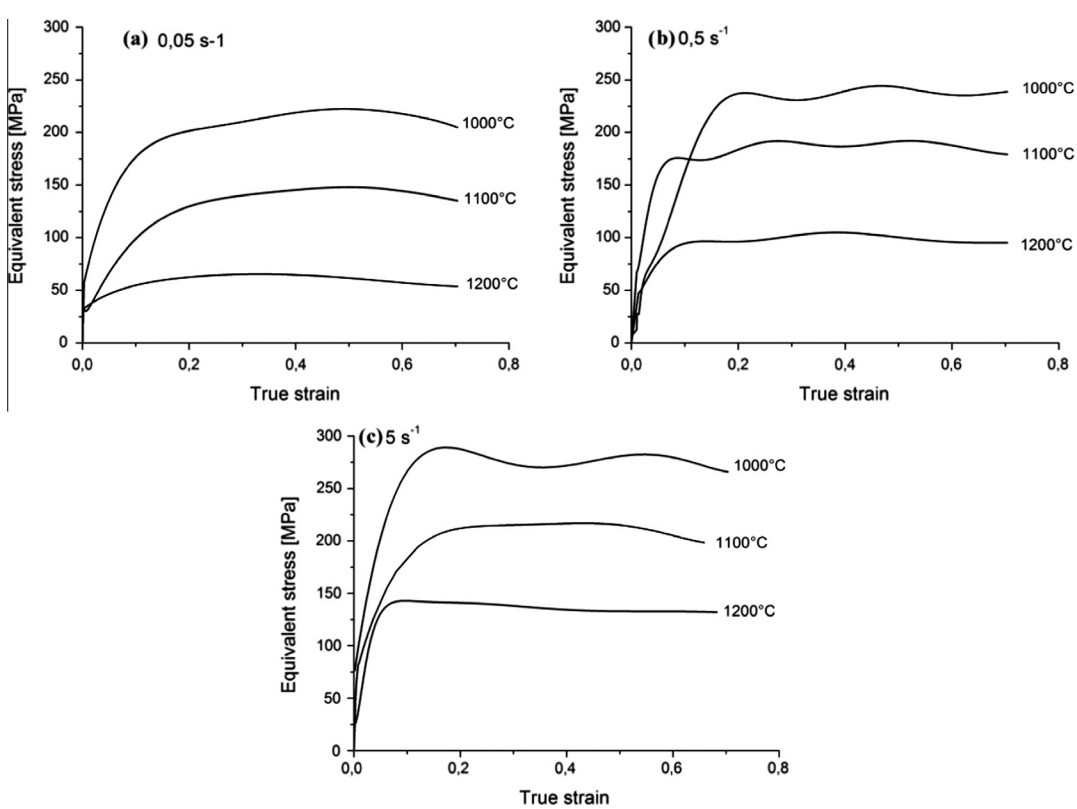


**Fig. 2.** Torsion flow curves of material 1 for different test conditions: (a) 0.05 $s^{-1}$, (b) 0.5 $s^{-1}$ and (c) 5 $s^{-1}$.

**Table 3**
Mechanical properties for the three investigated materials (peak flow stress and strain to failure).

| Temperature (°C) | Material 1 | | Material 2 | | Material 3 | |
|---|---|---|---|---|---|---|
| | $\sigma_{peak}$ (MPa) | $\bar{\varepsilon}_{failure}$ | $\sigma_{peak}$ (MPa) | $\bar{\varepsilon}_{failure}$ | $\sigma_{peak}$ (MPa) | $\bar{\varepsilon}_{failure}$ |
| 1000 | 220 | 0.75 | 150 | 0.98 | 145 | 0.5 |
| 1200 | 65 | 1.1 | 90 | 1 | 75 | 0.6 |

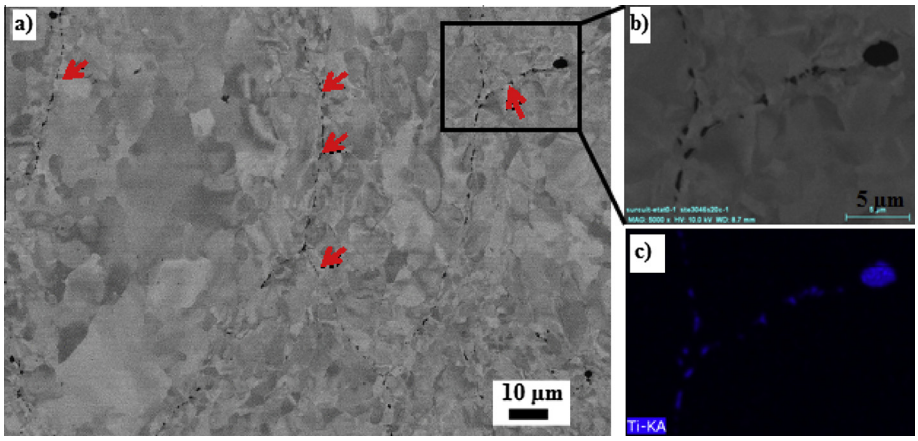


**Fig. 4.** (a) SEM image of material 3 before deformation. Red arrows show strings of precipitates at PPBs, (b) image of the boxed area and (c) titanium EDX spectra showing that precipitates are rich in Ti. (For interpretation of the references to colo in this figure legend, the reader is referred to the web version of this article.)

nucleate preferentially from those strings as can be shown in Fig. 5, which could explain the poor ductility of material 3.

From Table 3 it is also noticed that material 1 presents a higher flow stress at 1000 °C compared to material 2, with however a similar ductility.

It is worth noting that the reported levels of ductility are quite lower than those commonly observed for more conventional ferritic steels [16,18]. For HE, the large negative stress triaxiality during the process leads to a much better ductility than torsions tests [14,19].

### 3.2. Nano-precipitation

Nano-particles in the ODS materials were detected by small-angle neutron scattering (SANS) and transmission electron microscopy (TEM). Their characteristics in terms of mean diameter and volume density are reported in Table 4. Materials 1 and 2 present almost the same nano-oxides characteristics. On the other hand, material 3 exhibits the lowest number density and the highest mean diameter of nano-precipitates. These precipitation characteristics highlight the effect of the Ostwald repining during the heat treatment at 1350 °C for 3 h before the consolidation step.

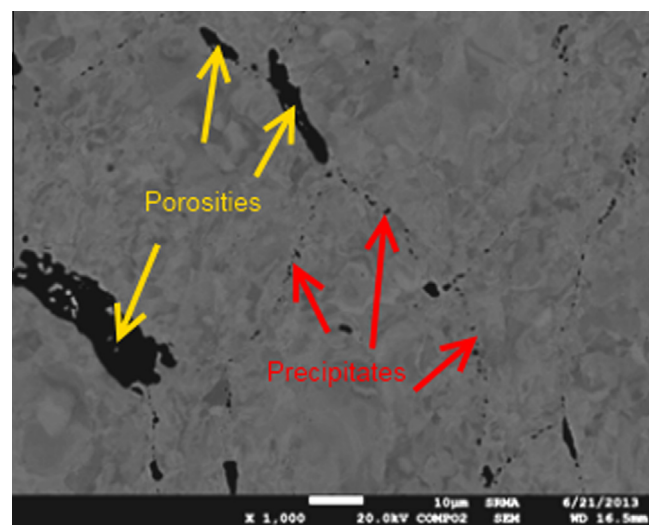


**Fig. 5.** SEM micrograph of material 3 deformed at 1200 °C showing damage porosities nucleated preferentially along strings of precipitates.

### 3.3. Microstructure evolution

Fig. 6 illustrates several EBSD maps of material 1. The microstructure of the as-received material (Fig. 6a) exhibits a double population of equiaxed grains, the largest ones having a size of a few µm, and the finest ones about 300 nm. The material does not show any crystallographic texture.

Fig. 6b reveals the obtained microstructure after deformation at 1000 °C and 0.05 $s^{-1}$. Some grains appear slightly elongated which conducts to a small increase of the average aspect ratio (Fig. 7).

At 1200 °C and 0.05 $s^{-1}$, and after a strain of 0.4 (Fig. 6c) corresponding to the maximum of the flow stress curve, the initial microstructure remains stable. Furthermore, Fig. 6d shows the microstructure in the fracture region after a strain of 1.1. The original grains still do not exhibit any elongation in the shearing direction, and no grain refinement is observed. As presented in Fig. 7, both the average grain size and the aspect ratio do not evolve very significantly with deformation. The texture is weak as well. The typical D2 component $\{\bar{1}\bar{1}2\}\langle 111\rangle$ expected in torsion tests of ferritic steels [18,22,23] is not observed (Fig. 8). XRD measurements performed on various torsion samples are reported in Fig. 9. For different conditions, the relative intensities of diffracted $\{hkl\}$ planes, normalized to $\{110\}$ planes, are quite similar to those of an isotropic bcc material. It means that the material deforms until fracture without developing any crystallographic texture. This result is consistent with the EBSD measurements shown in Fig. 6.

**Table 4**
Nanoparticles detected by SANS and TEM.

| | Technique | Metallurgical state | Mean diameter (nm) | Number density ($m^{-3}$) | Reference |
|---|---|---|---|---|---|
| Material 1 | SANS | Extruded bar | 3 | $10^{24}$ | [20] |
| Material 2 | SANS | Consolidated by SPS | 3.2 | $1.5 \cdot 10^{24}$ | [21] |
| Material 3 | TEM | Extruded bar | 8.9 | $1.1 \cdot 10^{22}$ | This study |

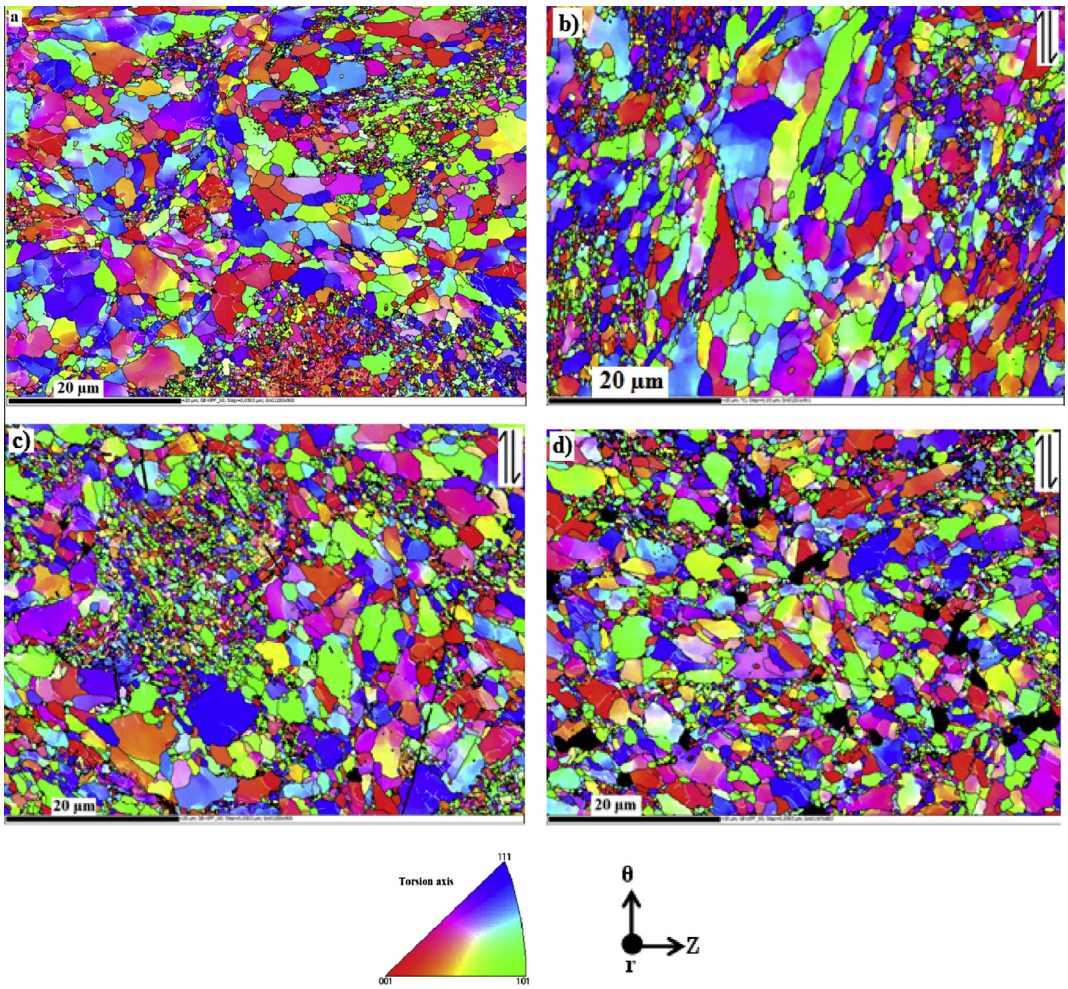


**Fig. 6.** Material 1, EBSD inverse pole figure maps, (a) as received material, (b) 1000 °C at 0.05 $s^{-1}$, rupture ($\bar{\varepsilon} = 0.75$), (c) 1200 °C at 0.05 $s^{-1}$, $\bar{\varepsilon} = 0.4$, (d) 1200 °C at 0.05 $s^{-1}$, rupture ($\bar{\varepsilon} = 1.1$). The white lines represent low angle grain boundaries with misorientation of 3–10°. The black boundaries have misorientation greater than 10°.

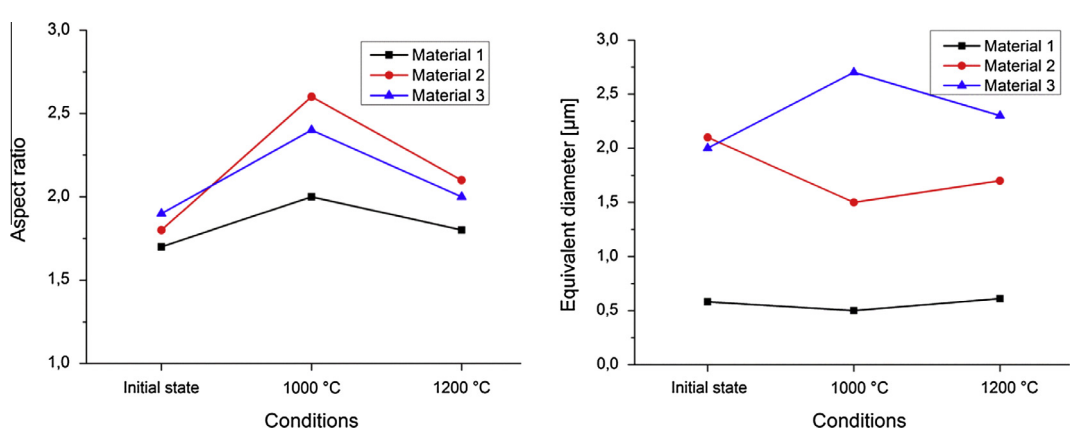


**Fig. 7.** Evolution of the average grain morphology and size during hot torsion at 0.05 $s^{-1}$, for the three investigated materials.

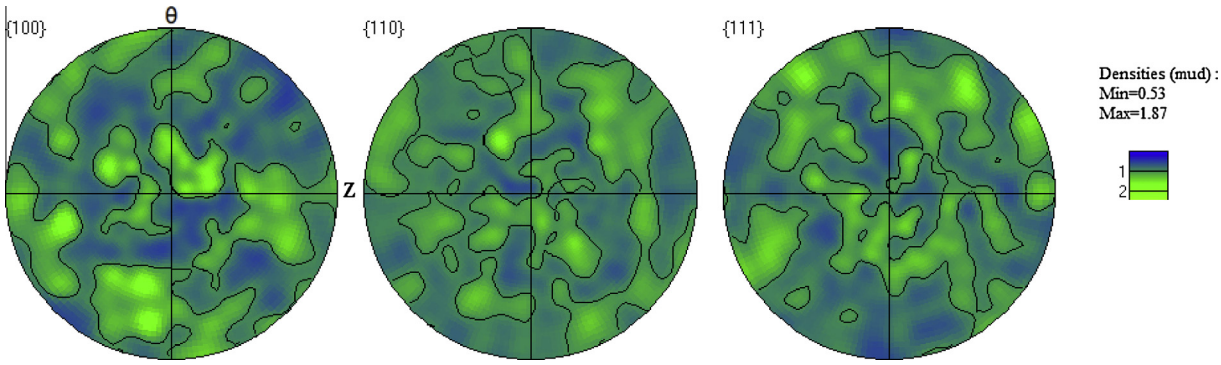


**Fig. 8.** Poles figures corresponding to Fig. 5c map.

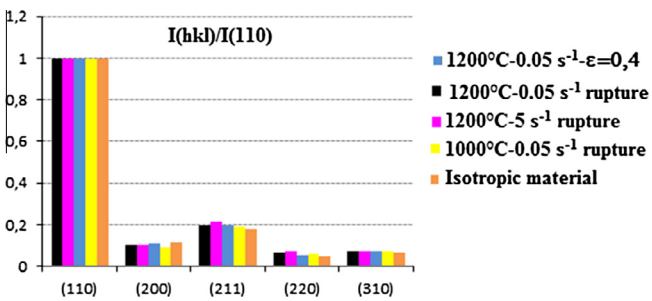


**Fig. 9.** Material 1, relative intensities of $I_{(hkl)}/I_{(1\,1\,0)}$ obtained by X-ray diffraction on selected deformed samples.

To understand the very weak textures obtained for ODS materials, XRD measurements were performed on a standard ferritic steel (AISI430) deformed in torsion in similar conditions, up to $\bar{\varepsilon} = 3$. The obtained poles figures presented in Fig. 10 show again a limited texture development. This suggests the existence of a threshold strain, about $\bar{\varepsilon} = 6$ according to Oliveira and Montheillet [18], from which the torsion texture appears in a bcc structure. Hence, the very low ductility of ODS steels in torsion, leading to early rupture, does not allow the development of a noticeable texture.

The rupture of ODS steels at high temperature is associated with growing of porosities along grain boundaries as can be seen in Fig. 6d. The black areas, corresponding to non-indexed pixels, reveal that damage initiated and developed mainly at grain boundaries. The poor ductility of these materials is therefore associated to intergranular damage.

The EBSD characterizations of materials 2 and 3 are reported in Figs. 11 and 12, respectively. Unlike material 1, material 2 presents less ultrafine grains (UFG) and a larger average grain size of about 2 μm (instead of about 0.5 μm, see Fig. 7). The reduced quantity of oxides leads to a lower proportion of these UFG. After deformation ($\bar{\varepsilon} = 0.98$) at 1000 °C and 0.05 $s^{-1}$ (Fig. 11b), some grains show a preferential elongation, leading to a slight increase in the average aspect ratio (from around 2 to 2.5), as presented in Fig. 7. This elongation trend is less present after deformation at 1200 °C and 0.05 $s^{-1}$ up to $\bar{\varepsilon} = 1$.

In a general way, the investigated samples show limited microstructural evolution during hot torsion. The same analysis applies to the material 3, as can be seen in Fig. 12 maps, and in Fig. 7. The increase of the nanoparticles size in this grade, from 3 to 9 nm, induced by the long heat treatment performed before the consolidation process (1350 °C/3 h), does not seem to impact strongly the deformation mechanisms. However, the pinning effects at grain boundaries are less effective, resulting in a larger average grain size after deformation.

Overall, the obtained results show that the studied materials have almost similar behavior under hot torsion straining. The microstructure shows limited evolution, which is quite unusual during hot working.

It is expected that ferritic steels undergo Continuous Dynamic Recrystallization (CDRX) during hot deformation [16,24]. This mechanism, generally encountered in high stacking fault energy materials, is associated with easy dislocation motion and efficient dynamic recovery. However, the studied materials do not indicate such behavior, at least in the investigated conditions. No significant refinement of the original microstructure is noticed, and few Low Angle grain Boundaries (LABs) are formed, even after large strains as shown in the EBSD maps and presented in Fig. 13.

In fact, the high particles density (up to $10^{24}$ particles/$m^3$) and the very small size of the nano-precipitates (a few nm), characteristics of ODS steels, could severely impede dislocation motion in the bulk of the grains. Moreover, small and large particles, could also lead to selective grain boundary pinning and explain the

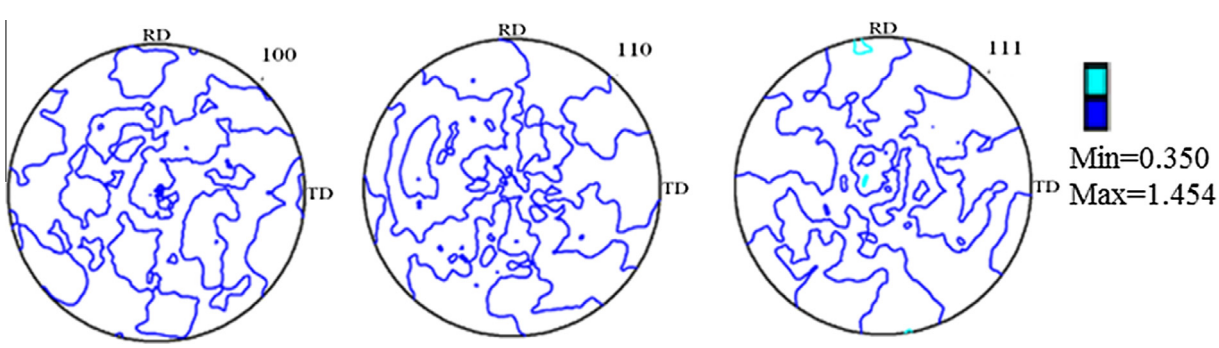


**Fig. 10.** XRD measurements of AISI430 texture after torsion deformation at 1200 °C and 0.1 $s^{-1}$ up to $\bar{\varepsilon} = 3$.

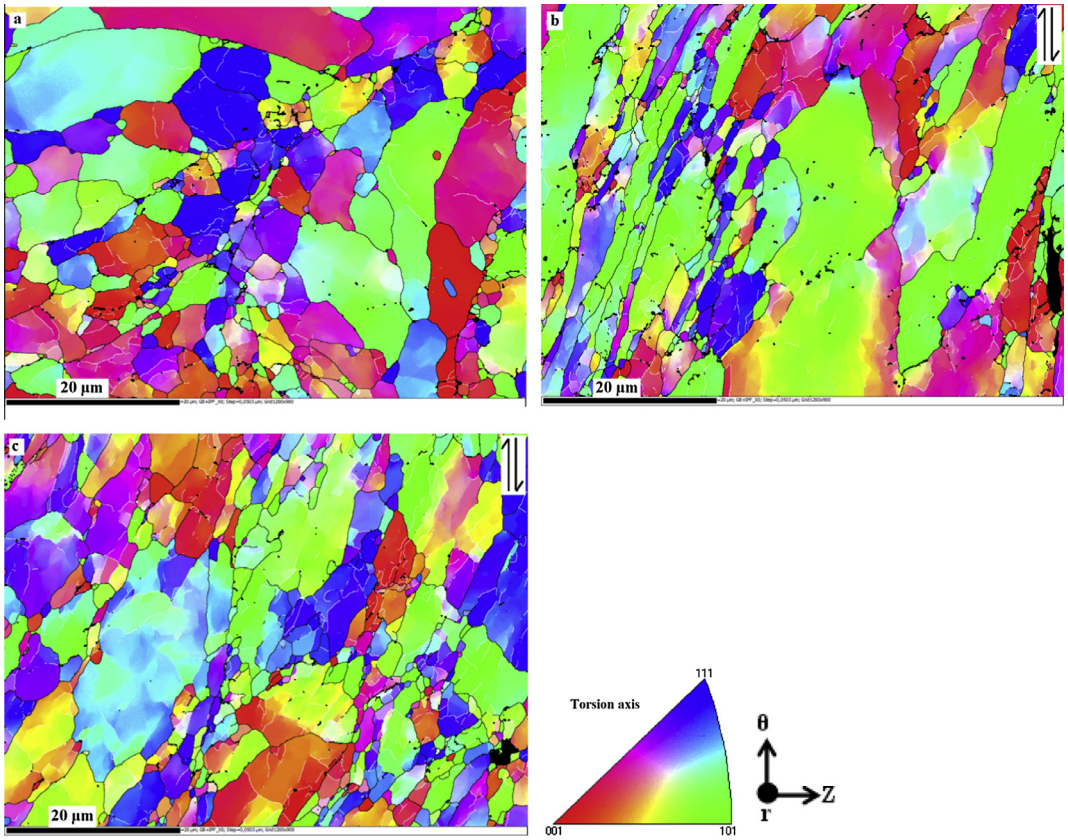


**Fig. 11.** Material 2, EBSD inverse pole figure maps, (a) as received material, (b) rupture at 1000 °C and 0.05 $s^{-1}$ ($\bar{\varepsilon} = 0.98$), (c) rupture at 1200 °C and 0.05 $s^{-1}$ ($\bar{\varepsilon} = 1$). The white lines represent low angle grain boundaries with misorientation of 3–10°. The black boundaries have misorientation greater than 10°.

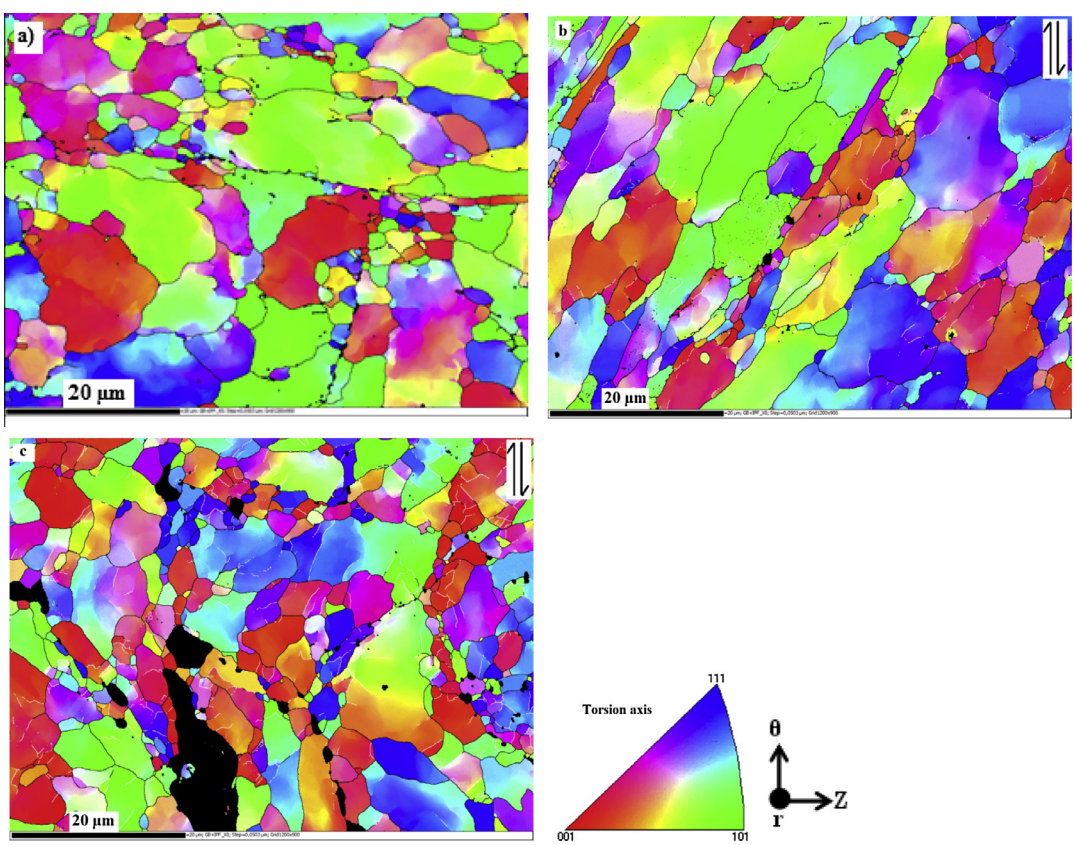


**Fig. 12.** Material 3, EBSD inverse pole figure maps, (a) as received material, (b) rupture at 1000 °C and 0.05 $s^{-1}$ ($\bar{\varepsilon} = 0.5$), (c) rupture at 1200 °C and 0.05 $s^{-1}$ ($\bar{\varepsilon} = 0.6$). The white lines represent low angle grain boundaries with misorientation of 3–10°. The black boundaries have misorientation greater than 10°.

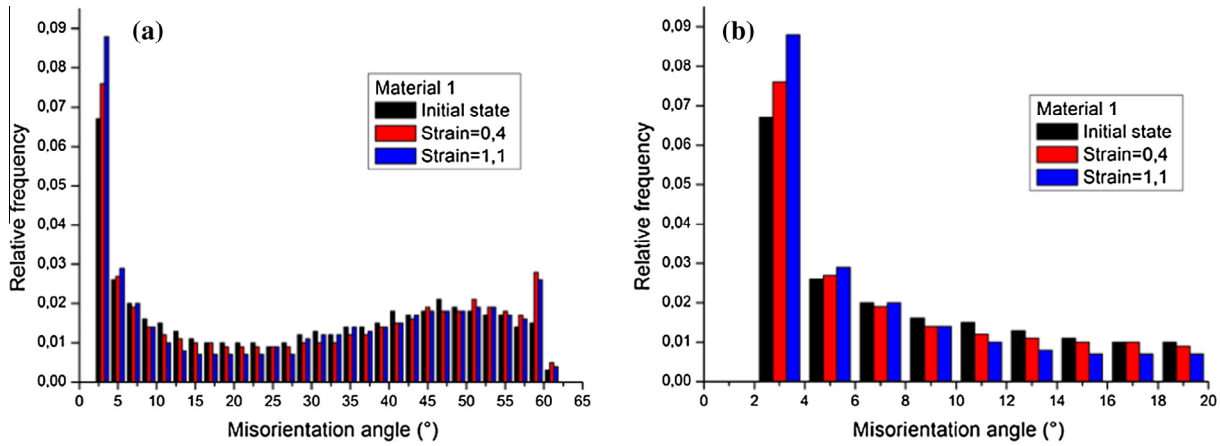


**Fig. 13.** The dependence of grain boundary misorientation distribution on strain level. Material 1 deformed at 1200 °C and 0.05 $s^{-1}$: (a) complete distribution and (b) zoom on the domain [0–20°]. A minimum misorientation cut-off of 2° has been used to eliminate excessive misorientation noise.

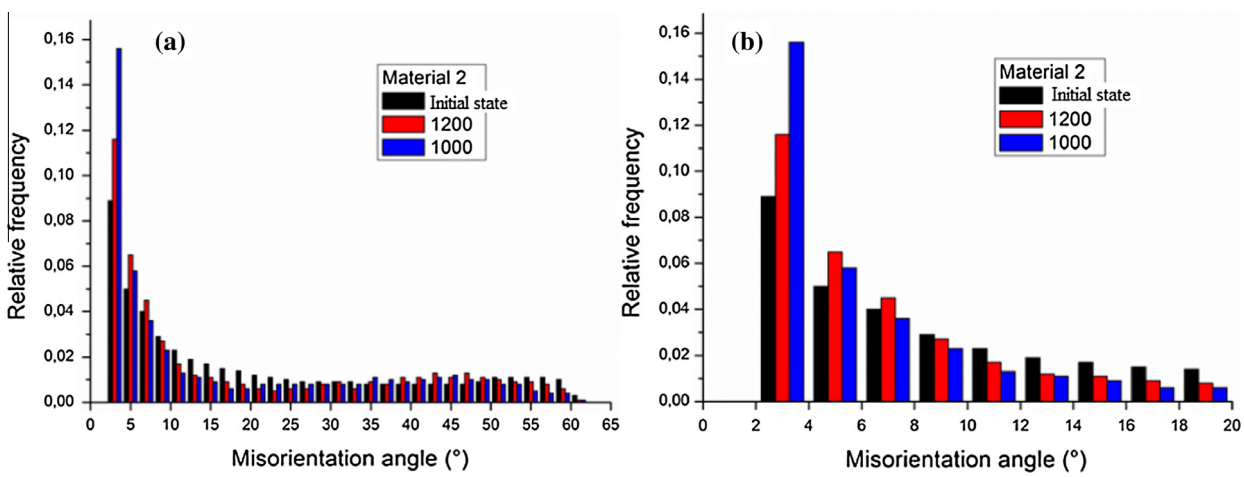


**Fig. 14.** The dependence of grain boundary misorientation distribution on temperature. Material 2 deformed at 1000 and 1200 °C, with a strain rate of 0.05 $s^{-1}$: (a) complete distribution and (b) zoom on the domain [0–20°]. A minimum misorientation cut-off of 2° has been used to eliminate excessive misorientation noise.

presence of a population of fine grains, as particularly apparent in material 1.

The dependence of grain boundary misorientation distribution on temperature is also presented in Fig. 14. A greater formation of LABs (<4°) is observed at 1000 °C compared to 1200 °C. This phenomenon could be explained by a thermally activated intergranular deformation mechanism. Indeed, the intragranular plasticity in the bulk of the grains is comparatively reduced, leading to a reduced creation of LABs and a lower aspect ratio of the grains (Fig. 7).

Damage may occur rapidly at the grain boundaries, due to locally intense dislocation activity and/or nucleation and growth of porosities in the presence of second-phase particles [9,17,25]. The occurrence of the grain boundary sliding at high temperature deformation of ODS ferritic steels was also reported by Sugino et al. in tensile tests at 800 °C and $10^{-4}$ $s^{-1}$ [26].

It is therefore assumed that intragranular plastic strain is limited by the nano-precipitates, and that the material significantly deforms by accommodation at grain boundaries, which leads to intergranular damage unless prevented by large negative stress triaxiality. The weak morphologic texture evolutions observed after the torsion tests are consistent with this scenario. On the contrary, after HE, significant textures have been formed [9,10], which is a sign of an important intragranular dislocation slip activity. Thus, it is expected that stress triaxiality can influence the competition between intergranular and intragranular deformation mechanisms.

## 4. Conclusion

Metallurgical phenomena involved in hot forming of three ODS ferritic steels have been investigated. Torsion testing at various temperatures and strain rates has been associated to SEM-EBSD and X-ray diffraction techniques to characterize the samples microstructures. The following conclusions have been reached.

- Under hot working conditions, the ODS materials follow a typical viscoplastic behavior: the flow stress increases with increasing strain rate and decreasing deformation temperature.
- The torsion flow stresses of tested materials are higher than those commonly observed in similar conditions for standard ferritic steels. Their ductility however is significantly reduced because of very fine precipitates that can be effective barriers to the motion of dislocations. This highlights the role of nano-precipitates dispersion on the mechanical behavior of ODS steels.
- The EBSD analyses of deformed samples from material 1 reveal a stable heterogeneous grain size microstructure, consisting of small and large grains. Except for the damage, the microstructure evolution is limited.

- Both EBSD and X-ray diffraction results show that tested samples do not develop a significant crystallographic or morphologic texture, with strains as high as 1, 3.
- Materials 2 and 3 behave similarly to material 1 (with however larger grain sizes), which means that neither the quantity of Ti and $Y_2O_3$ added to the matrix (material 1 vs. material 2) nor the size of the nano-precipitates and their volume density (material 2 vs. material 3) affect significantly the deformation mode at high temperature.
- Unlike the standard ferritic steels, the studied ODS materials do not show evidence of dynamic recrystallization under the investigated conditions.
- For all tested materials, plastic strain accommodation mechanisms at grain boundaries are suspected to compete with intragranular dislocation slip, due to the very high nano-precipitates density. These accommodation mechanisms are associated to a strong intergranular damage development, which explains the limited ductility observed in torsion tests.

The analysis of other strain paths with different stress triaxialities is under way. It is expected that stress triaxiality could influence the competition between intragranular and intergranular deformation mechanisms.

This study was achieved in the frame of the collaboration between the CEA, AREVA NP, and EDF.

## References

[1] P. Dubuisson, Y. De Carlan, V. Garat, M. Blat, J. Nucl. Mater. 428 (2012) 6–12.
[2] Y. De Carlan, J.L. Bechade, P. Dubuisson, J.L. Seran, P. Billot, A. Bougault, T. Cozzika, S. Doriot, D. Hamon, J. Henry, M. Ratti, N. Lochet, D. Nunes, P. Olier, T. Leblond, M.H. Mathon, J. Nucl. Mater. 386–388 (2009) 430–432.
[3] S. Ukai, 4.08 – Oxide Dispersion Strengthened Steels, in: J.M.K. Rudy (Ed.), Comprehensive Nuclear Materials, Elsevier, Oxford, 2012, pp. 241–271.
[4] P. Yvon, F. Carré, J. Nucl. Mater. 385 (2009) 217–222.
[5] R.L. Klueh, J.P. Shingledecker, R.W. Swindeman, D.T. Hoelzer, J. Nucl. Mater. 341 (2005) 103–114.
[6] J. Malaplate, F. Mompiou, J.L. Béchade, T. Van Den Berghe, M. Ratti, J. Nucl. Mater. 417 (2010) 205–208.
[7] P. Olier, J. Malaplate, M.H. Mathon, D. Nunes, D. Hamon, L. Toualbi, Y. de Carlan, L. Chaffron, J. Nucl. Mater. (2011)
[8] R. Kasada, S.G. Lee, J. Isselin, J.H. Lee, T. Omura, A. Kimura, T. Okuda, M. Inoue, S. Ukai, S. Ohnuki, T. Fujisawa, F. Abe, J. Nucl. Mater. 417 (2011) 180–184.
[9] A. Steckmeyer, M. Praud, B. Fournier, J. Malaplate, J. Garnier, J.L. Béchade, I. Tournié, A. Tancray, A. Bougault, P. Bonnaillie, N. Baluc, J. Nucl. Mater. 405 (2010) 95–100.
[10] M. Serrano, M. Hernandez-Mayoral, A. Garcia-Junceda, J. Nucl. Mater. 428 (2012) 103–109.
[11] M. Serrano, M. Hernandez-Mayoral, A. Gracia-Junceda, J. Nucl. Mater. 428 (2012) 103–109.
[12] L. Toualbi, C. Cayron, P. Olier, R. Logé, Y. de Carlan, J. Nucl. Mater. 442 (2013) 410–416.
[13] D. Sornin, T. Grosdidier, J. Malaplate, I. Tiba, P. Bonnaillie, N. Allain-Bonasso, D. Nunes, J. Nucl. Mater. 439 (2013) 19–24.
[14] D. Sornin, A. Karch, F. Barcelo, Int. J. Mater. Form. (2013), http://dxdoi.org/10.1007/s12289-013-1156-5. in press.
[15] D.S. Fields, W.A. Backofen, Proc. ASTM 57 (1979) 583–591.
[16] S.-I. Kim, Y.-C. Yoo, Met. Mater. Int. 8 (2002) 7–13.
[17] M. Praud, F. Mompiou, J. Malaplate, D. Caillard, J. Garnier, A. Steckmeyer, B. Fournier, J. Nucl. Mater. 428 (2012) 90–97.
[18] T.R. Oliveira, F. Montheillet, Mater. Sci. Forum 495–497 (2005) 477–482.
[19] B. Gaudout, Thèse de doctorat. Ecole des Mines CEMEF (2009) Code ID: 5021.
[20] L. Toualbi, C. Cayron, P. Olier, J. Malaplate, M. Praud, M.H. Mathon, D. Bossu, E. Rouesne, A. Montani, R. Logé, Y. de Carlan, J. Nucl. Mater. 428 (2012) 47–53.
[21] X. Boulnat, D. Fabregue, M. Perez, M.H. Mathon, Y. Decarlan, Metall. Mater. Trans. A-Phys. Metall. Mater. Sci. 44A (2013) 2461–2465.
[22] C. Castan, F. Montheillet, A. Perlade, Scripta Mater. 68 (2013) 360–364.
[23] F. Montheillet, M. Cohen, J.J. Jonas, Acta Metall. 32 (1984) 2077–2089.
[24] A. Oudin, P.D. Hodgson, M.R. Barnett, Mater. Sci. Eng., A 486 (2008) 72–79.
[25] A. Steckmeyer, V.H. Rodrigo, J.M. Gentzbittel, V. Rabeau, B. Fournier, J. Nucl. Mater. 426 (2012) 182–188.
[26] Y. Sugino, S. Ukai, B. Leng, Q. Tang, S. Hayashi, T. Kaito, S. Ohtsuka, ISIJ Int. 51 (2011) 982–986.